Journal of Colloid and Interface Science 612 (2022) 467–478

Contents lists available at ScienceDirect

Journal of Colloid and Interface Science

journal homepage: www.elsevier.com/locate/jcis

On the growth of the soft and hard protein corona of mesoporous silica particles with varying morphology

Inga Kuschnerus [a,b], Kalpeshkumar Giri [c,d], Juanfang Ruan [a,e], Yanan Huang [f], Nicholas Bedford [g], Alfonso Garcia-Bennett [c,d,*]

[a] Electron Microscope Unit, Mark Wainwright Analytical Centre, University of New South Wales, Sydney, NSW, Australia
[b] School of Materials Science and Engineering, University of New South Wales, Sydney, NSW, Australia
[c] Department of Molecular Sciences, Macquarie University, Sydney, NSW, Australia
[d] Centre for Nanoscale and BioPhotonics, Macquarie University, Sydney, NSW, Australia
[e] School of Biotechnology and Biomolecular Sciences, University of New South Wales, Sydney, NSW, Australia
[f] Department of Chemistry, Fudan University, Shanghai, China
[g] School of Chemical Engineering, University of New South Wales, Sydney, NSW, Australia

GRAPHICAL ABSTRACT

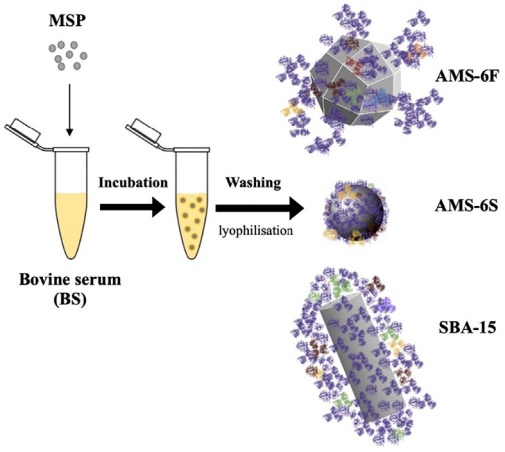

ARTICLE INFO

Article history:
Received 19 July 2021
Revised 23 December 2021
Accepted 24 December 2021
Available online 31 December 2021

ABSTRACT

The characterization of the protein corona has become an essential part of understanding the biological properties of nanomaterials. This is also important in the case of mesoporous silica particles intended for use as drug delivery excipients. A combination of scattering, imaging and protein characterization techniques is used here to assess the effect of particle shape and growth of the reversible (soft) and strongly bound (hard) corona of three types mesoporous silica particles with different aspect ratios. Notable differences in the protein composition, surface coverage and particle agglomeration of the protein corona-particle complex point to specific protein adsorption profiles highly dependent on exposed facets and aspect ratio. Spherical particles form relatively homogeneous soft and hard protein coronas (approx.10 nm thick) with higher albumin content. In contrast to rod-shaped and faceted particles, which possess soft coronas weakly bound to the external surface and influenced to a greater extent by the

* Corresponding author at: School of Natural Sciences, Macquarie University, Sydney, NSW, Australia.
E-mail address: alf.garcia@mq.edu.au (A. Garcia-Bennett).

https://doi.org/10.1016/j.jcis.2021.12.161
0021-9797/© 2022 Elsevier Inc. All rights reserved.

particle morphology. These differences are likely important contributors to observed changes in biological properties, such as cell viability and immunological behaviour, with mesoporous silica particle shape.
© 2022 Elsevier Inc. All rights reserved.

1. Introduction

Mesoporous silica particles (MSPs) are being considered as excipients in pharmaceutical formulation for advanced drug delivery. Their ability to encapsulate high amounts of drug compounds within the pores, specifically poorly soluble compounds stabilized in their non-crystalline form, combined with their low toxicological profile and mechanical strength make MSPs unique amongst functional nanostructured excipients [1–4]. MSPs in the size range of 100–1000 nm especially excel in oral drug formulations, transdermal, [5][6] ocular and for intraperitoneal drug administration [7,8]. When colloidal particles are dispersed in physiological media, either as part of a disintegrating oral tablet in the gastrointestinal tract or as an injected formulation in contact with blood plasma, they exhibit properties associated with a high degree of protein opsonization resulting in the formation of an enzymatic or protein corona (PC) surrounding the particle. The new biomolecular corona ensues, affects the function of the MSPs to a large extent [9–10]. The PC may interfere with their drug release properties and therapeutic efficiency after gastrointestinal adsorption, [11–12] cellular uptake, [13] the particle's immunological properties, [14–15] and eventual clearance in the body [16–17]. In parallel, differences in the particle morphology of MSPs have been found to influence cytotoxicity, [18] their ability to cause haemolysis, [10] and their *in vivo* biodistribution after intravenous administration [19–21]. For these reasons, the *hard* surface bound irreversible corona and the *soft* PC have been the focus of recent MSP research [22–26]. Specifically, the soft PC is thought to induce significant agglomeration, mask the particles surface chemistry and decrease the interaction of cell membrane receptors with surface functional groups [27–29]. Some early studies have focused on the effect of mesopore size on the composition of the PC but do not consider the role of particle shape. Vidaurre-Agut *et al.* observed differences in PCs around spherical MSPs with varying mesopore diameter. Smaller mesopores adsorb more apolipoprotein AII, and larger mesopores ($\geq$14 nm) adsorb higher amounts of complement factor C3, when the particles were incubated in protein containing phosphate buffered saline (PBS) [22]. Ma *et al.* exposed spherical and rod-shaped MSPs of varying pore diameters to either albumin, fibrinogen and globulin, evaluating changes to the protein structure and adsorption via Fourier-transform infrared (FTIR) spectroscopy [29]. The adsorption rate of albumin and immunoglobulin onto all MSPs decreased sequentially as the particle surface curvature decreased from spherical to rod-shaped particles. The initial adsorption rate of fibrinogen increased with decreased curvature due to the rod-shaped properties of fibrinogen. This study however does not take into account the complexity of muti-protein media. Increases in the amount of immunoglobulins and albumin adsorbed in the hard PC of MSPs after plasma and serum incubation on rods compared to spherical particles were recently reported [26]. The longitudinal axis of the rods, where the curvature is only 1-dimensional (1d), is proposed as the reason for the greater protein packing density. Surprisingly, this study does not consider the potential for protein adsorption within the mesopores, and how this may influence the resulting protein-corona complex on the exterior of the particle.

A detailed proteomic classification and comparison of the PC of different MSPs with faceted, spherical and elongated morphologies has been reported recently [10,30–32]. There are large similarities in the hard PC of all serum-incubated silica particles (in bovine or human plasma). They contain albumin, apolipoproteins, complement proteins, α-2-macroglobulin and gelsolin in the top 10 proteins irrespective of the pore size, shape, incubation time or surface charge (from silanol or functional amine groups) of the particle being tested. Surprisingly the top 10 proteins account for over 75% of the total protein content of the PC. A different PC is detected when MSPs are incubated in human whole blood, [33] with albumin as the only component present in all the tested media. Some proteins are only observed after incubating particles in a specific media at high concentrations, as for example the detection of haemoglobin after incubation in fetal bovine serum (FBS). Coagulation proteins (*e.g.* thrombospondin and prothrombin) appear in higher abundance in amine functionalized particles with net positive surface charge [34]. Clemments *et al.* conclude that low molecular weight proteins are primarily adsorbed on the surface of MSPs, [23] whilst PEGylation of the silica surface prevents protein adsorption. This is a desirable particle property which may result in a low immune cell association [21,35]. However, after protein incubation the silica particle-corona complex could be considered as an additional tool in drug formulation that may enhance drug delivery, promote cellular targeting and promote specific immunomodulatory effects, as has been recently demonstrated [21,36–39].

In this work, we focus on studying the dynamic changes to the soft and hard PC by following changes to the porosity, surface chemistry, particle size and shape of MSPs using a variety of *ex-situ* techniques, such as small angle X-ray scattering (SAXS), surface enhanced Raman spectroscopy (SERS) and dynamic light scattering (DLS), supported with cryo-transmission electron microscopy (cryo-TEM) and proteomic analysis of the soft and hard PCs. Similar methodology has been used previously by Sheibani et al., [40] who showed the soft and hard PC around 100 nm carboxylate polystyrene (PS)–COOH via cryo-TEM. Moreover, Yadav et al. [41]. have used small angle neutron scattering (SANS) and DLS to show the size dependent adsorption behaviour of different proteins around non-porous silica particles.

This study explores how preferential adsorption of proteins on specific particle facets, and within the mesopores can determine the composition of the PC of MSPs. An MSP with a 3-dimensional (3d)- cubic mesoporous silica structure and cylindrical pores (anionic surfactant templated mesoporous silica material 6 (AMS-6)) is used, which can be synthesised with spherical and faceted morphologies [42]. Materials are termed AMS-6S (spherical morphology, 4.9 nm pore size) and AMS-6F (faceted, 4.7 nm pore size). The MSP Santa Barbara Amorphous-15 (SBA-15) with 2d-hexagonal cylindrical pores (10.7 nm) and rod-shaped particle morphology is also used in this work to allow comparisons based on aspect ratio. It is important to note that whilst SBA-15 possesses rod-type morphology, the surface along the axis of the mesopores is curved and structured, due to open mesopores exposed to the exterior of the particle [43]. The assumption that a relatively flat cylindrical surface facilitates a high packing density may thus be oversimplified in the case of the SBA-15 particles prepared here.

2. Experimental

2.1. Chemicals and solutions

The following chemicals and solutions were purchased from Merck Australia and used as received: *N*-Lauroyl-L-

Alanine ≥ 99.0% purity, 3-aminopropyl triethoxysilane (APES) ≥ 98% purity, tetraethyl orthosilicate (TEOS) ≥ 99% purity, 3-aminopropyl trimethoxysilane (APMS) 97% purity, Pluronic P123, hydrochloric acid (HCl, reagent grade 37%), sterile bovine serum (BS) (adult, origin USA) as well as phosphate buffered saline (PBS) tablets.

Lysis buffer and MOPS SDS (3-(*N*-morpholino) propane sulfonic acid, sodium dodecyl sulphate) running Buffer (≥99.5%) were purchased from Thermo Fisher Scientific Australia. Formic acid (2%) and acetonitrile (50%) solution buffers A (2% v/v acetonitrile, 0.1% v/v formic acid) and B (99.9% v/v acetonitrile, 0.1% v/v formic acid) were prepared in house.

2.2. MSP synthesis

The AMS-6S MSPs were synthesized following and already described procedure [44]. Briefly, in a polyvinyl chloride (PVC) bottle, 1.25 g of the surfactant (*N*-Lauroyl-L-Alanine, C_{12}AlaA) was added to 250 ml deioinized water. The mixture was stirred for 12 h at 80 °C at 200 rpm. The stirring speed was increased to 1000 rpm for 10 min, before adding 1.25 g of the co-structure directing agent APES and 6.25 g of the silica source TEOS. Afterwards, the mixture was stirred for another hour at 1000 rpm and then reduced to 500 rpm for 12 h. After filtration and initial drying of the material, the surfactant was removed by calcination at 550 °C for three hours in flowing air.

The AMS-6F MSPs were synthesized using a modified protocol to the one described above [42]. In a polypropylene bottle, 0.8 g surfactant (*N*-Lauroyl-L-Alanine) was dissolved in 160 g deionized water and left without stirring in a closed bottle at 80 °C for 24 h. After one day, 0.68 g of the co-structure directing agent APMS under vigorous stirring at 80 °C for 1 min. Then, 0.51 g of a polymeric non-ionic dispersant (Pluronic P123) and 60 g of deionized water was added in separate polypropylene bottle and stirred at room temperature for 12 h. Afterwards, the P123 solution was added to the surfactant solution and stirred at 80 °C for 12 min. After 12 min, 4.15 g of the silica source (TEOS) was added and stirred for 10 min. After 10 min the solution was stored in the closed bottle for 48 h under static conditions at 80 °C. The material was then hydrothermally treated at 100 °C for 24 h, filtered, and dried overnight at 95 °C. The surfactant was removed by calcination at 550 °C as described above.

The SBA-15 MSPs were also synthesized using a previously published protocol [45]. In a polypropylene bottle, 3.9 g of P123, 135 g deionized water, 9.8 g HCl and 8.2 g of TEOS were added and stirred at 40 °C for 20 h. Afterwards, the bottle was closed in an oven at 100 °C for 48 h. The material was then filtered and dried overnight at 60 °C. The surfactant was removed by calcination at 550 °C as described above.

2.3. Protein corona formation

The MSPs samples were incubated with bovine serum (BS) for different times (10 min, 30 min and 120 min): 1 ml of BS was added to 1 mg MPS in 1.5 ml Eppendorf tubes (Eppendorf, Hamburg, Germany) and placed on a shaker at 200 rpm at room temperature. The hard PC was isolated via temperature-controlled centrifugation for 15 min, 14000 rpm (4 °C). The supernatant was discarded and the remaining MSP pellets re-dispersed in Milli-Q water and either washed again or prepared for following characterization processes. Calcined MSPs were incubated in 100% BS, for different time periods at room temperature (termed in minutes T_{10}, T_{30} and T_{120}) before centrifugation and washing steps (termed $W_{1\text{-}3}$), which are conducted to remove loosely adsorbed proteins on the particle surface (the soft PC). The remaining protein layer after three washing cycles is termed hard PC. To prepare the incubated mesoporous MSP-corona complex for characterization by scanning electron microscopy (SEM), thermogravimetric analysis (TGA), and nitrogen adsorption/desorption isotherm the sample was lyophilized. For lyophilization the samples were frozen in their Eppendorf tubes after the last washing process at −80 °C and then placed in a lyophilization glass container (Martin Christ Freeze Dryers, Osterode am Harz, Germany). The sample was placed under vacuum overnight at −50 °C and 0.1 mbar in a freeze dryer (Martin Christ, Osterode am Harz, Germany). For characterization by DLS, zeta-potential measurement and cryo-TEM the sample were redispersed in Milli-Q water (1 ml) and stored at −30 °C.

2.4. Protein corona and particle characterization

2.4.1. Statistical analysis

Unpaired Student's t-tests were used for statistical analysis of DLS measurements using excel (Microsoft, USA). A p-value < 0.05 was considered statistically significant. Values with error bars stated in figures and tables refer to the mean ± standard deviation (SD).

2.4.2. Proteomics/LC-MS

MSP-corona complex samples were mixed with 20 µl of lysis buffer and boiled at 95 °C for 5 min. Afterwards, samples were loaded into NUPAGE 4–12% BT GEL of 12 wells (Life Technologies, Carlsbad, USA). The gel was run for 55–60 min at 200 mV in 20 times diluted in MOPS SDS Running Buffer (10x). The samples were then stained with Coomassie Brilliant Blue R-250 Staining Solutions Kit (Bio-Rad, Hercules, USA) for two hours, followed by washing in Milli-Q water for two to three days.

After the SDS-PAGE procedure, gel-bands were excised from the gel and dehydrated using acetonitrile, followed by vacuum centrifugation. Dried gel bands were treated with 10 mM dithiothreitol and alkylated with 55 mM iodoacetamide. Afterwards, the gel bands were washed, alternating between 25 mM ammonium bicarbonate and acetonitrile. The whole procedure was then repeated, and the gel bands were again dried via vacuum centrifugation. Samples were digested with trypsin overnight at 37 °C. Peptide extraction was performed using a formic acid (2%) and acetonitrile (50%) solution. The extracted peptide solution was dried via vacuum centrifugation and peptides were then reconstituted in 0.1% formic acid solution.

The peptide analysis was performed using liquid chromatography-tandem mass spectrometry (LC-MS/MS) on a Q-Exactive hybrid Quadrupole Orbitrap mass spectrometer (Thermo Fisher Scientific, Waltham, USA). An in-house packed trap (Halo® 2.7 µm 160 Å ES-C18, 100 µm × 3.5 cm) and analytical column (Halo® 2.7 µm 160 Å ES-C18, 75 µm × 10 cm) were used. Prior to the MS, high performance liquid chromatography (HPLC) separation was performed using nanoflow liquid chromatography EASY-nLC™ II (Thermo Fisher Scientific, Waltham, USA). A linear gradient of buffers A (2% v/v acetonitrile, 0.1% v/v formic acid) and B (99.9% v/v acetonitrile, 0.1% v/v formic acid) was used for the elution of peptides. The starting gradient was 1–50% buffer B for 50 min followed by increase in buffer B concentration from 50 to 85% for two minutes and column washing at 85% of buffer B for eight minutes. The flow rate was kept constant at 300 nl/min during the gradient. The mass spectrometry spectral acquisition was performed in the scanning range of 350–2000 m/z in positive mode. For the tandem mass spectrometry analysis, HCD fragmentation of the top 10 most intense precursor ions was performed at a normalized collision energy of 30% (Xcalibur, Thermo Fisher Scientific, Waltham, USA). Three technical replicates per samples were performed.

2.4.3. Dynamic light scattering (DLS)

DLS experiments were performed with a Zetasizer ZS (Malvern Instruments, Worcestershire, UK), with a 173° detector angle, at 25 °C with a He-Ne laser (633 nm, 4mW output power) as a light source. MSP samples (20 μl, 1 mg/ml) were mixed with 1 ml filtered PBS (Fig. 3) or Milli-Q water (**Figure S3**) and filled into disposable folded capillary cell (DTS1070) (Malvern Instruments). For AMS-6S and AMS-6F samples, hydrodynamic diameter values were directly obtained from the measurements. However, since conventional DLS measurements do not accurately display the hydrodynamic diameter for rod-shaped particles, [46] the dimensions of the length of the SBA-15 samples (L) and the diameter (d) (Scheme 1) were analysed according to the following. The Stokes-Einstein equation is used in DLS to determine the particle size, as follows:

$$D_t = \frac{k_B T}{6\pi\eta R_h}$$

where, D_t is the translational diffusion coefficient of the particles, k_B is the Boltzmann constant, T is the temperature of the liquid, η is the dynamic viscosity of the liquid (Milli-Q water and PBS), and R_h is the hydrodynamic radius of the particles. The size, R_h of particles can be obtained by measuring the value of D_t. For non-spherical particles, a correction factor, $G(p)$, to the Stokes-Einstein equation is required, [47]

$$D_t = \frac{k_B T}{6\pi\eta \frac{L}{2}} G(p)$$

This correction factor is highly dependent on the geometrical features of the particles. Hence, the data was treated using the correction factor for prolate particles (ellipsoids) as described by Schmitt *et al.*, [47] where $L > d$:

$$G(p) = \frac{1}{\sqrt{1-p^2}} \ln\left(\frac{1+\sqrt{1-p^2}}{p}\right)$$

and where $p = d/L$, otherwise referred to as the aspect ratio of the rods, and $L/2$ is referred to as the major axis radius. Thus, two parameters are needed to describe the dimensions of SBA-15 via DLS, namely the translational diffusion coefficient D_t and the aspect ratio p. Although the size measured for non-spherical particles via conventional DLS is inaccurate, D_t can be derived directly from the experimental data and was here averaged for six measurements. It is important to note, that all DLS measurements were done at a fixed angle of 173° and not at multiple angles, which would provide more accuracy. The value for p was measured by SEM and averaged for 60 particles (see Table 1) and is in good agreement with the value used for similar particles in [47]. Since both values contain uncertainties, the propagation of uncertainty $G(p)$, was taken into account while calculating the error ($u_{G(p)}$) for L and d, where:

$$\Delta G(p) = \frac{dG(p)}{dp}\Delta p \;\Rightarrow u_{G(p)} = \left|\frac{dG(p)}{dp}\right| u_p$$

where u_p is the standard deviation of the aspect ratio p determined from 60 SEM images. Hence, $u_{G(p)}$ was set as 0.35. To combine the error of $G(p)$ with the standard deviation of D_t (u_{Dt}) to get the error for $L/2$ (u_L), the gaussian error propagation law was used, which leads to the following relation:

$$\left(\frac{u_L}{\frac{L}{2}}\right)^2 = \left(\frac{u_{Dt}}{D_t}\right)^2 + \left(\frac{u_{G(p)}}{G(p)}\right)^2$$

Values obtained from calcined SBA-15 are tabulated in Table 1. The same method was used to obtain values of L and d in protein incubated particles of SBA-15.

2.4.4. Zeta-potential measurement

The zeta-potential of the MSPs was measured with a Zeta Sizer ZS (Malvern Instruments, Worcestershire, UK) in 1 ml of filtered Milli-Q water. For the measurements, a disposable folded capillary cell (DTS1070, Malvern Instruments, Worcestershire, UK) was utilized.

2.4.5. X-ray diffraction (XRD)

Powder X-ray diffraction (XRD) studies were performed on pure calcined MSP samples to evaluate the crystallinity using a Bruker D8 Discover diffractometer (Bruker, Billerica, USA). As X-Ray source, Cu-Kα radiation was utilized (λ = 1.5406 Å). The diffraction patterns were recorded between 1 and 8° 2θ. The data was collected and analysed with the DIFFRAC.SUITE™ software.

2.4.6. Nitrogen adsorption/desorption isotherm

Nitrogen adsorption/desorption isotherms were obtained at a temperature of −196 °C using liquid nitrogen with a TriStarII instrument (Micromeritics, Norcross, USA). The surface area is calculated using the BET equation in a relative pressure range between 0.05 and 0.2. Prior to the measurements, the MSP sample was degassed under vacuum using the VacPrepTM061 by (Micromeritics, Norcross, USA) to remove adsorbed moisture, for approximately 12 h at room temperature.

2.4.7. Surface enhanced Raman spectroscopy (SERS)

For SERS, gold substrate microscope slides (Dynasil, Newton, USA) were used. Approximately 1 mg of lyophilized sample was spread on the gold substrate and measurements were immediately performed with a Sierra Raman instrument (Snowy Range Instruments, Laramie, USA) using a laser power of 30mW, a wavelength of 785 nm and an integration time of 60 s. For each spectrum 10 measurements were recorded and averaged. Background measure-

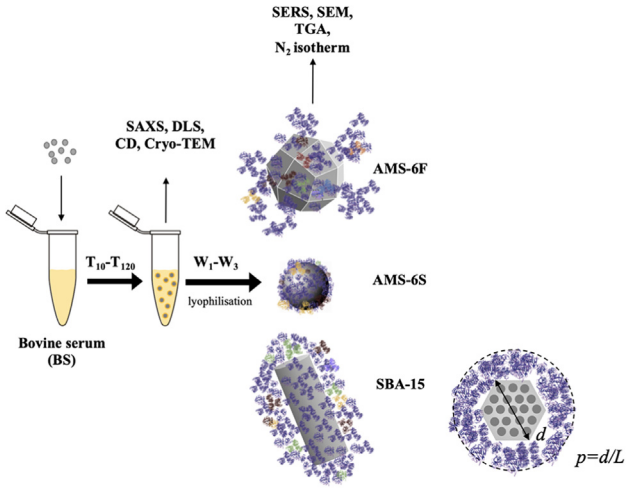

Scheme 1. Representation of the formation of a hard PC around MSP incubated in BS, with different particle shapes. For SBA-15, d is the diameter of the MSP, in the plane perpendicular to the pore direction; and L is the rod-length along.

Table 1
Structural data for pure SBA-15 derived from SEM (statistics over 60 particles with the error given by the SD).

MSP	L (nm)	d (nm)	p
SBA-15	2336 ± 499	419 ± 140	0.19 ± 0.07

ments were obtained under the same condition as for the sample measurements and subtracted.

2.4.8. Small angle X-ray scattering (SAXS)

SAXS measurements were performed at the Small Angle/Wide Angle X-ray beamline of the Australian Synchrotron. The energy of the incident X-ray beam was set at 12 keV and the beam size was 250 μm horizontal × 450 μm vertical. The maximum flux at the samples was 8×10^{12} photons per second. The SAXS data were recorded by a 2d Dectris-Pilatus 200 K detector, positioned at 2.68 m from the sample. Background scattering of the solvent and the experimental setup was subtracted from data. To model the size distribution the *Irena* package of the software Igor Pro version 8.02 (WaveMetrics, Portland, USA) was used [48]. SAXS measurements were conducted with 0.1 mg/ml MSPs at a range of BS concentrations (0.25, 0.5 and 2.5 mg/ml). The scattering length densities (SLD) for each component were derived as described previously by Spinozzi *et al.*, [49] with values (expressed in the units 10^{-6}Å^{-2}) of 8.47, 11.9 and 9.4 for MSPs, BS and water, respectively. Scattering profiles of calcined AMS-6S and AMS-6F in water could be adequately fitted with a Gaussian distribution of a spheroid in a dilute system with the largest population centred at 164 nm and 317 nm, respectively. Samples of AMS-6S and AMS-6F incubated in BS were best fitted with a Gaussian distribution of a core–shell spheroid. The size distribution increases with the formation of a soft PC around both AMS-6 particles, but only for AMS-6F does it continue to increase with increasing BS concentration. For both materials, the shell thickness remains relatively constant with increasing BS concentration, with average values of 30.2 and 5.7 Å for AMS-6S and AMS-6F, respectively. For SBA-15 a Schulz-Zimm cylinder distribution in a dilute system was utilized, [50] and for incubated samples a Schulz-Zimm distribution of core–shell cylinders in combination with a second population of a Gaussian distribution of spheroids best fitted the data. All fitting parameters that were used for the samples can be found in **Table S5** and **Table S6** of the Supporting Information.

2.4.9. Thermogravimetric analysis (TGA)

For the TGA measurements, a sample amount of approximately 3 mg was placed in an aluminum crucible of a TGA device by Netzsch (STA 449 F3 Jupiter, Netzsch, Selb, Germany). The sample was analysed under airflow with 10 ml/min increasing the temperature from 40 to 900 °C with 10 °C/min. The percentage of each protein identified in the proteomic analysis as a function of molecular weight ($MW_{protein}$), was multiplied by the overall mass of absorbed proteins determined via TGA [22].

2.4.10. Scanning electron microscopy (SEM)

The lyophilized sample was spread on a metal stub using carbon adhesive and inserted in the sample chamber of the SEM. SEM images were obtained using a JSM 7100F FESEM field emission scanning electron microscope (Jeol, Tokyo, Japan). The images were recorded at 2.5 keV to 1.5 keV using gentle beam setting and LED detector, without the use of any coating.

2.4.11. Cryo-transmission electron microscopy (TEM)

The 4uL sample solution was applied as a droplet onto the glow-discharged grids (R2/2 Quantifoil copper grids, Germany) in a humidity chamber at a constant humidity of 80%. The excess dispersion was removed by blotting with filter paper for two to three seconds. The grid was then plunged into liquid ethane with a temperature of −180 °C. Cryo-TEM imaging was performed on a Talos Artica TEM (Thermo Fisher Scientific, Waltham, USA) using an acceleration voltage of 200 keV.

Circular dichroism (CD) spectroscopy

Circular dichroism (CD) experiments were performed on a Jasco J-810-150S spectrometer (Jasco Inc., Tokyo, Japan) (230 V 50/60 Hz and 270 W) using a 1 ml cylindrical quartz cell (Helma, Singapore) with 1 mm pathlength at room temperature over the range of 180 to 300 nm. A minimum of six scans were averaged. BS and MSP samples were dispersed in Milli-Q water at a ratio of 0.25 mg/ml to 0.1 mg/ml, respectively.

3. Results and discussion

The structural and textural properties of calcined MSPs are tabulated in Table 2**,** together with the hydrodynamic particle size, zeta-potential and PDI determined by DLS in PBS. AMS-6S particles possess a spherical morphology (Fig. 1a), with a hydrodynamic particle size distribution of 547 nm. AMS-6F particles have a trapezoidal icositetrahedron morphology, characterized by 24 {2 1 1} facets **(**Fig. 1d**)**, [42] with a larger hydrodynamic particle size centred at 911 nm. The {2 1 1} facets expose different pore structural features to the exterior of the particle than in AMS-6S [51]. Particles of SBA-15 have a rod-like morphology with a hydrodynamic particle length centre around 2336 nm. Powdered X-ray diffractograms are shown in the Supporting Information **Figure S1**. Note the significant difference in the pore size distribution of SBA-15, which is more than twice the diameter of the two AMS-6 materials (4.6 and 4.5 nm). The 3d porous networks of AMS-6 also results in a larger surface area (>750 m^2/g) than for the 2d mesopores of SBA-15 (527.8 m^2/g). The calcined SBA-15 material prepared possesses a relatively small amount of microporosity, with a contribution of 43.8 m^2/g to the total surface area of the material.

To observe changes in scattering as a result of the formation of a soft and hard BS corona around the mesoporous particles, SAXS measurements were conducted. Fig. 2 shows the SAXS scattering profiles of MSPs dispersed in solutions containing BS and in water, together with their form factor fittings. For the sake of clarity, the SAXS graphs have been scaled as follows: AMS-6S and AMS-6F 0.25 mg/ml BS, 0.5 mg/ml BS and 2.5 mg/ml samples are scaled by the factor of 40, 1000 and 10000, respectively. SBA-15 0.5 mg/ml BS and 2.5 mg/ml BS samples are scaled by the factor of

10,000 and 100000, respectively. Pure BS 0.5 mg/ml and 2.5 mg/ml samples are scaled by the factor of 100 and 1000, respectively. A complete set of values and fitting parameters are included in **Table S1 and S2** of the Supporting Information. The resulting radii size distribution of SBA-15 decreases initially with the formation of a PC. However, with increasing BS concentration the size distribution increases. The cylindrical shell of the SBA-15 increases as a function of BS concentration in the studied range, with a value of 104.6 Å at the higher concentration of 2.5 mg/ml. Interestingly, the shell thickness stays constant at 0.25 and 0.5 mg/ml, but triples at 2.5 mg/ml. Data at even higher concentrations (5.0 mg/ml) was collected, however the agglomeration was too severe to model it adequately. Overall, the formation of a PC at different concentrations of BS influences the scattering in the higher q-range (0.05–0.2 Å^{-1}), overlapping with the scattering peak of the MSP core. The derived scattering volume fraction distribution curves (**Figure S2** in the Supporting Information) show that particle agglomeration is inhibited at higher concentrations for AMS-6S, whereas the opposite effect is observed for AMS-6F. This data also indicates that SBA-15 does not form a significant hard PC at low BS concentrations (0.25 – 0.5 mg/ml), as suggested by a poor fitting of a *core shell cylinder model* at small q-ranges (0.002 – 0.02 Å– [1],Fig. 2c). Instead, a better fit is obtained for the scattering by considering independently the BS protein overlapping the SBA-15 scattering, which may be indicative of unbound protein. At a concentration of 2.5 mg/ml the *core–shell cylinder model* can be used to describe the scattering curve of the SBA-15-corona complex, indicating the

Table 2
Structural and textural properties of MSPs in this work.

MSP (*meso*-structure)	Unit cell (Å)*	Particle shape	d_{DLS} (in PBS, nm)	Zeta-potential (mV)	PDI (in PBS)	W_{pore} (nm)¥	V_{pore} (cm^3/g)¥	S_{BET} (m^2/g)¥
AMS-6S 3d-cubic	109.7	sphere	547 ± 62	−27.8 ± 1.5	0.41 ± 0.07	4.5 ± 0.3	0.87 ± 0.03	797.7 ± 3.3
AMS-6F 3d-cubic	113.7	icositetrahedron	911 ± 38	−23.1 ± 0.8	0.52 ± 0.06	4.6 ± 0.1	0.78 ± 0.02	767.8 ± 3.3
SBA-15 2d-hex	100.5	rods	2336 ± 499Φ	−22.5 ± 0.1	0.37 ± 0.03	10.7 ± 1.1	0.90 ± 0.06	527.8 ± 2.7

*Values obtained from powder XRD (**Figure S1**), ¥ values from nitrogen adsorption isotherms (**Figure S2**), Φ value for the rod length, *L*. Results show mean ± SD of three measurements.

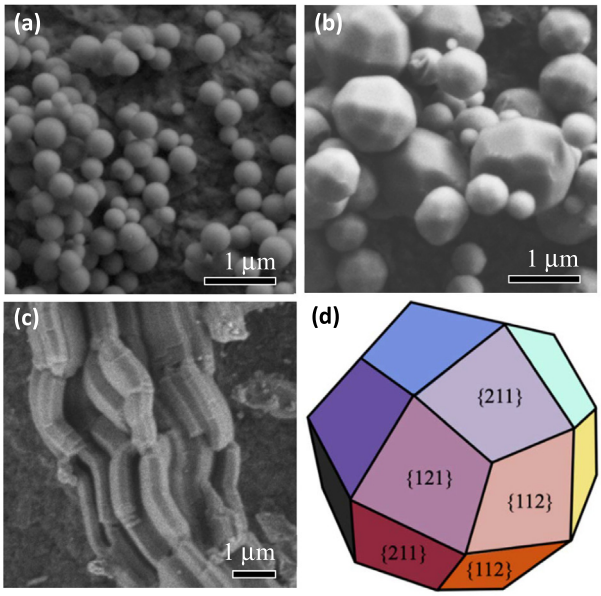

Fig. 1. SEM images of **(a)** AMS-6S, **(b)** AMS-6F and **(c)** SBA-15. **(d)** Model of the trapezoidal icositetrahedron morphology of AMS-6F highlighting the {2 1 1} family of facets.

formation of a stable hard PC. All in all, the SAXS data indicates an interaction between the proteins and AMS-6S as well as AMS-6F, as seen in the changes of the scattering profile in the higher q-range (0.02 – 0.2 $Å^{-1}$).

Using DLS, no significant increase in the particle size distribution of AMS-6S is observed immediately due to the formation of a PC ($W_{1\text{-}2}$) at any of the incubation time periods. An increase is observed upon removal of the loosely bound proteins at $T_{10}W_3$ with values increasing to 677 nm (Fig. 3a).

Similarly, AMS-6F does not significantly change in particle size upon the formation of a soft or hard PC, except at the $T_{30}W_1$ incubation, which shows an initial decrease in particle size to 706 nm, followed by a sequential increase to 932 nm after removal of the soft PC at $T_{30}W_3$ (Fig. 3b). The hydrodynamic length of SBA-15 particles (Fig. 3c) initially increases to 1222 nm due to the formation of a PC. Sequential increases in size are observed as the soft PC is removed, through the washing cycles. Increase in size due to the removal of unbound proteins can be rationalized from the standpoint of an increase in agglomeration.

In contrast, the formation of a hard PC following the washing cycles does not have as much influence in the particle agglomeration of AMS-6S or AMS-6F. When DLS measurements are performed in (Milli-Q) water, only AMS-6S remains relatively stable in size through the washing steps, whilst a large amount of agglomeration is observed in AMS-6F (**Figure S3b**). Noteworthy is the deagglomeration of incubated SBA-15 in water after a single washing cycle at all incubation times, in contrast to measurements in PBS, which is what we suspect the results of sedimentation of the particles in water. Presumably, a higher degree of charged proteins are adsorbed on the surface in water, shielding the {100} planes of the hexagonal rods of SBA-15 from interacting with each other and agglomerating.

Measurements of zeta-potential show that the net particle surface charge becomes more neutral for all three MSPs after incubation in BS (Fig. 3d-f) in agreement with previous reports [33,52]. This change is more pronounced for SBA-15 particles, which become more neutral after every washing step, consistent also with the small increases in agglomeration observed from DLS (Fig. 3c). A progressive change in agglomeration and zeta-potential are indicative of specific protein layers being removed with washing steps. The hard PC of SBA-15 at $T_{120}W_3$ has a zeta-potential value of −5mV whilst that of AMS-6S and AMS-6F retains a more negatively charged surface at −15 and −10 mV, respectively.

The total amount of proteins adsorbed in the hard PC was estimated from TGA and correlated with nitrogen adsorption data obtained on hard PC MSP lyophilized samples (**Figure S4-S5, Table S3-S4**). All TGA curves show at least two main decomposition peaks. The peak between 250 and 420 °C can be related to the removal of proteins weakly-bound via van der Waals forces [53]. The peak between 420 and 800 °C is assigned to the removal of proteins strongly bound via electrostatic interactions over multiple points [54–55]. An additional decomposition peak in the TGA profiles of AMS-6F and SBA-15,particularly prominent at $T_{30}W_3$ samples, in the temperature range of 190–250 °C is observed. This cannot be assigned to any specific protein from TGA alone, however, this decomposition peak could arise from proteins in the hard PC that are not directly interacting to the MSP surface but through weaker protein–protein interactions in between particles of AMS-6F and SBA-15.

All samples undergo a reduction in mesopore size, mesopore volume and specific surface area as a function of prolonged BS incubation in comparison to the initial calcined materials, indicating protein adsorption within the mesopores (Fig. 4a). However, even after prolonged BS incubation ($T_{120}W_3$), MPSs retain their mesoporosity and high surface areas (Fig. 4b). The normalized spectral counts (NSpC) of detected proteins in the hard PC, obtained from LC-MS analysis are shown as a relative percentage of the total protein adsorption in Fig. 4c. However, there seems to be no significant difference between the mesopore volume and specific surface area of the different incubation times. This indicates that the role of the mesoporosity is minimal with respect to protein adsorption within the pores. This is likely due to an early blocking the surface mesopores which prevents protein diffusion within the particle. The molecular weight fraction in the hard PC of MSPs is dominated by smaller proteins in the range of 1–50 kDa, amounting to over 40% of the detected proteins. This agrees with previous observations that suggest the prevailing pres-

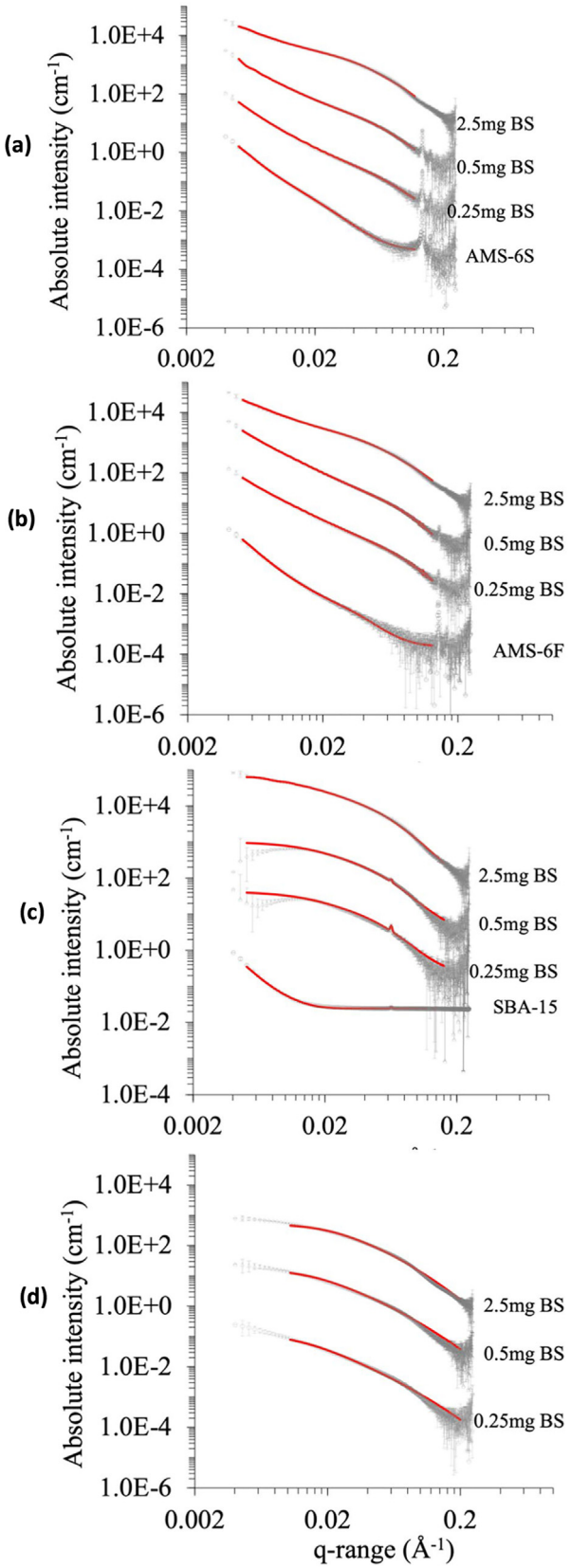

Fig. 2. **(a-c)** Background subtracted SAXS curves of pure 0.1 mg/ml MSPs, MSPs with BS at different concentrations and **(d)** pure BS in water (0.25–2.5 mg/ml). Black curves represent the form factor fitting.

ence of low molecular weight proteins in the PC of other nanostructured materials, irrespective of porosity [10,23,56]. The smaller 1–50 kDa range of adsorbed proteins is depleted in SBA-15 with prolonged incubation time. Larger proteins (>200 kDa) increase by a few percent for all materials with incubation time. Previously reported proteomics analysis shows the hard PC of AMS-6 and SBA-15 to be dominated by α-2-macroglobulin (30.28 kDa), albumin (69.32 kDa), apolipoprotein-AI proteins

(167.57 kDa) and complement C3 (187.25 kDa) [32]. Multiplying the percentage ratio by the total protein mass calculated from TGA allows to estimate the molecular mass distribution of proteins in the PC of MSPs (Fig. 4d). The hard PC of AMS-6S remains most homogenous in terms of molecular weight distribution and total protein content. The highest protein content adsorbed is measured in the hard PC of SBA-15 at 0.35 mg/m^2, owing to increased adsorption of proteins < 100 kDa. The high protein adsorption of SBA-15 for smaller proteins has been reported previously, with higher adsorption kinetics favoured for smaller proteins, including bovine serum albumin (BSA) (dimensions 4 nm × 4 nm × 4 nm) at capacities over 450 mg/g under conditions where minimization of repulsive electrostatic interactions between adsorbed proteins and adsorbent surface are achieved, when the protein isoelectric point (pI) is close to the pH of the media [57].

The SERS spectra recorded on the soft (W_1) and the hard PC (W_3) of lyophilized MSP samples, as a function BS incubation time are shown in Figure 5. The spectra for calcined MSPs show no distinct peaks whilst that of pure BS shows characteristic bands Figure S6 [58]. The SERS spectra of MSP-corona complexes show peak

broadening, consistent with significant conformational changes in the adsorbed proteins. In contrast, these bands are detectable at all incubation time points in SBA-15 and AMS-6S. Only bands positioned between 698 and 712 cm^{-1} (COO^-, symmetric bend), 752–757 cm^{-1}, 858–863 cm^{-1} (Pyr, pyrrole breathing) are visible at all incubation times for AMS-6F-corona complexes. BSA is the most abundant protein in BS making up > 50% of the protein content, with approximately 24% of amino acid residues in BSA comprised of glutamic and aspartic acid (Glu and Asp), and 3.5% from Phe [58]. It is thus possible to associate the 1003 cm^{-1} to a predominance of BSA in the soft and hard PC of MSPs. Bands at 692–698 cm^{-1} (COO^- deformation from Glu and Asp), [59] are also weaker for AMS-6F than for the other two MSPs. Overall, the SERS spectra, whilst difficult to interpret, suggests the PC of AMS-6F is different, if not in composition most likely in thermal stability, which is also suggested by the additional decomposition peak in the TGA data. Higher thermal stability could also be caused by conformational changes of the proteins due to strong electro-static interactions with the MSP surface. Investigation via CD show structural changes for proteins in BS in presence with all MSPs, albeit minute for AMS-6S and AMS-6F and more profound for SBA-15 (see **Figure S8**), which demonstrate the formation of a hard PC.

Cryo-TEM (Fig. 6) and SEM images (Fig. 7) recorded on MSPs incubated with BS show contrast features on the external particle surface associated with adsorbed proteins. Particularly the SEM images show the different severeness of agglomeration for the different types of MSPs. For instance, AMS-6S shows less stacking than AMS-6F and SBA-15, which appears to be most agglomerated (see Fig. 7). Control cryo-TEM images of pure BS can be found in **Figure S7**. The soft PC is easily visible around AMS-6F and SBA-15 particles. The soft PC of SBA-15 is characterized by a darker contrast associated with proteins extending to a few 100 nm beyond the particles' surface. The soft PC of AMS-6F particles shows a dendritic contrast extending over larger distances. Only a weak diffuse contrast is observed for the soft PC of AMS-6S. Cryo-TEM images recorded on the hard PC however show higher contrast, with a homogeneous protein coating approximately 3 nm in thickness clearly and consistently visible surrounding AMS-6S particles (Fig. 6d). The hard PC of AMS-6F and SBA-15 show faint contrast. This is primarily found parallel to the pore direction in SBA-15

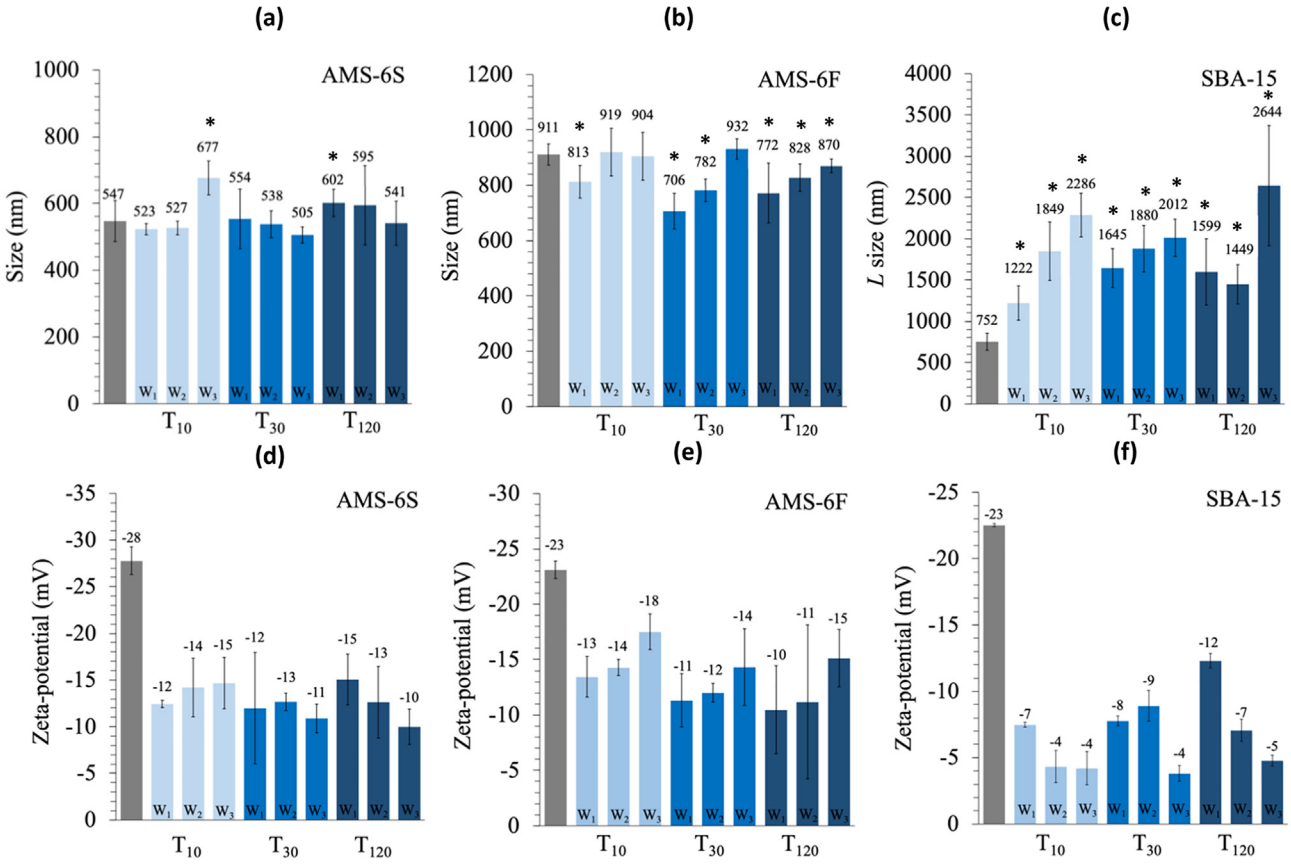

Fig. 3. **(a-c)** DLS measurements and **(d-f)** zeta-potential measurements of calcined and BS incubated MSPs at different time points (T_{10} to T_{120} in minutes) showing values for soft (after one or two washing steps, W_1-W_2) and hard PC (W_3). Results show the mean ± SD of six measurements. Asterisk markers represent measurements with significant size difference to the pure particle size measured by *t*-test ($p < 0.05$).

(Fig. 6e-f). Recently, Kokkinopoulou *et al.* assessed changes to the morphology of spherical polystyrene particles (approximate diameter of 150 nm) coated with a PC using cryo-TEM and tomography, differentiating between the soft and the hard PC prepared after incubation in human serum [60]. Similarities in the dendritic nature of the contrast observed for the soft PC and its dimensions are observed between MSPs and polystyrene particles. Interestingly, values obtained here from cryo-TEM for the thickness of the hard PC of AMS-6S are somewhat smaller than for the non-porous polystyrene particles (10–20 nm) reported for polystyrene particles. Contrast is also observed around the entire periphery of the particles, even when individual proteins (clusterin, apolipoprotein A1 or IgG) were used to form a hard PC.

The amount of proteins adsorbed per unit surface area is largest for the incubated SBA-15 samples. However, AMS-6F showed the second largest specific protein adsorption, somewhat larger than AMS-6S, (see Table 1). It is unlikely that this difference is mesopore size, pore structure nor surface area. Adsorption isotherm curves for AMS-6 hard PC samples show a decrease in the total mesoporous volume, but this occurs without a significant change in the capillary condensation step; neither in quantity adsorbed nor in relative pressure (**Figure S5**). Thus, the decrease in adsorption after the protein incubation is more likely due to a lower fraction of MSP adsorbent (per unit weight) in the hard PC samples than to protein adsorption within the mesopores. Further, the surface chemistry does not seem to be a key factor since the zeta-potential measurements of all incubated MSPs remain largely the same similar (Fig. 3d-f) [30].

Interestingly, the type H1 hysteresis of SBA-15 does vary slightly in terms of relative pressure and closure point (desorption branch) in the hard PC samples, indicating some adsorption within the mesopores. SBA-15 is also a significantly larger particle than both AMS-6 MSPs. Previous studies report larger amounts of protein adsorption in smaller particle sized MSPs [22]. In this work SBA-15 showed adsorption of smaller molecular weight proteins only at shorter incubation times (over 60% of proteins at $T_{10}W_3$) in the hard PC, but not at longer incubation times. This is consistent with a pore size effect, rather than particle size. The PC of AMS-6S is more thermally stable than that of AMS-6F and SBA-15, which decomposes at lower temperatures from thermogravimetric analysis. This indicates a larger amount of weaker electrostatic protein–protein interactions, as opposed to stronger silica surface-protein interactions [61]. Whilst modelling of the SAXS data shows a significantly thicker protein shell for AMS-6S than for AMS-6F, with thickness of 30.2 and 5.7 Å, the population 1 size distribution for AMS-6F samples almost doubled in size with increasing protein concentration, from approximately 30 nm to 62 nm. The SLD's of protein and silica are very similar, which makes it difficult to distinguish contributions to the scattering from the PC in the shell. This is especially so for shells that may not be homogenous in thickness such as those suspected for the elongated and weakly bound PC of AMS-6F. Supporting these differences, SERS spectra (Figure 5) suggest a higher protein content in the soft and hard PC of AMS-6S than AMS-6F.

Morphological differences are also observed from cryo-TEM images of both AMS-6 samples which lead us to conclude that the surface of AMS-6F act as specific protein adsorption sites. This has been observed in other nanoparticles such as platinum, [62] but should be of special interest in the design of mesoporous mate-

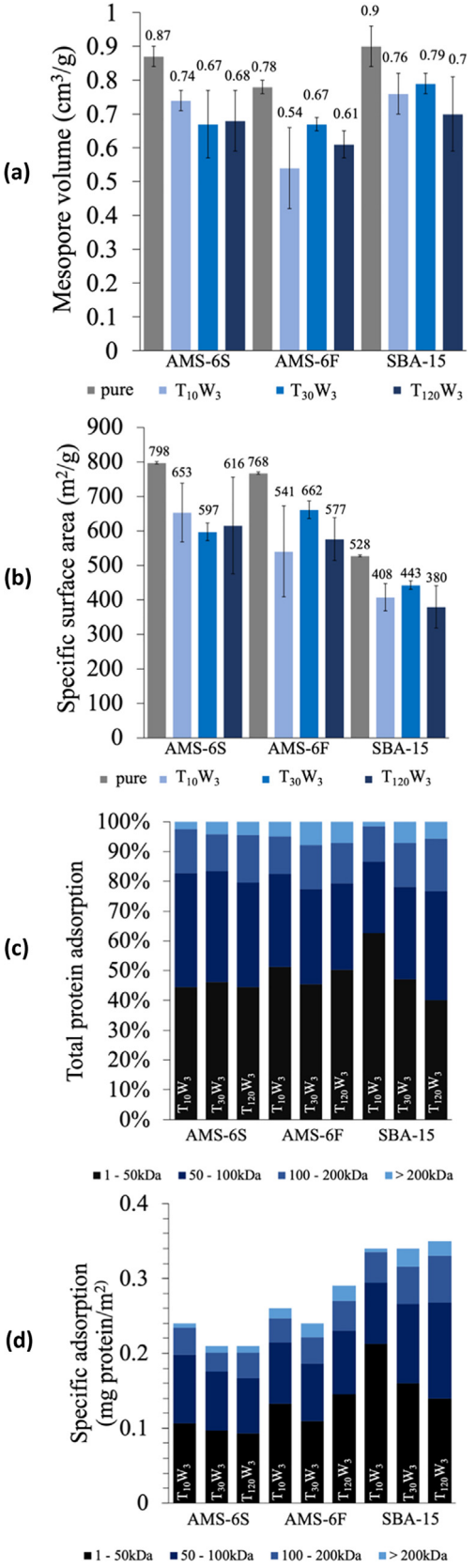

Fig. 4. **(a)** Specific surface area of MSPs without and with PC. **(b)** Decrease in mesopore volume as a function of incubation time. **(c)** Distribution of protein molecular weight fractions in the hard PC of MSPs. **(d)** Specific protein adsorption per unit surface area for each molecular fraction. Error bars represent the SD of three measurements.

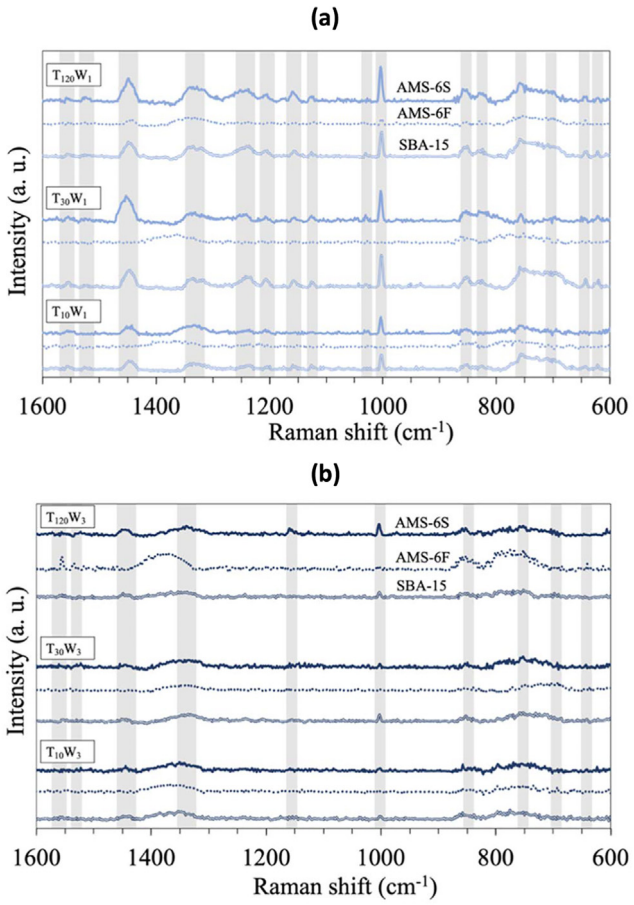

Fig. 5. Surface-enhanced Raman Scattering (SERS) of **(a)**, the soft (W1), and **(b)** hard (W3) corona of MSPs determined as a function of incubation time and washing steps. Tentative band assignments are tabulated in **Table S5-S7**.

rials for drug delivery application, where the control of drug release and cellular interactions could be designed through protein incubation protocols.

4. Conclusions

In this work we present for the independent characterization of the soft and hard PC of mesoporous silica particles with cubic and hexagonal mesoporous structures. The composition, surface coverage and particle agglomeration of the protein corona-particle complexes of mesoporous materials is highly dependent on particle aspect ratio and exposed facets. All mesoporous particles studied adsorbed proteins within their mesopores, with the larger pore SBA-15 (10.7 nm), showing a wider variation in the molecular weight protein composition with incubation time, than the smaller mesopore AMS-6 particles (4.5 nm). A rapid de-agglomeration of mesoporous SBA-15 particles is observed upon incubation with serum.

The soft corona of AMS-6 particles with trapezoidal icositetrahedron morphology is characterized by weakly bound adsorption on the {2 1 1} family of facets, leading to a dendritic protein corona. In contrast, the PC of spherical AMS-6 particles is homogenous in thickness (ca. 3 nm), more stable to washing procedures and contains a higher amount of albumin. These results agree with the approximate dimensions expected for BSA interacting with metal oxide surfaces [58,59].

Overall, our work suggests that the protein and biomolecular corona of mesoporous materials may be carefully engineered by

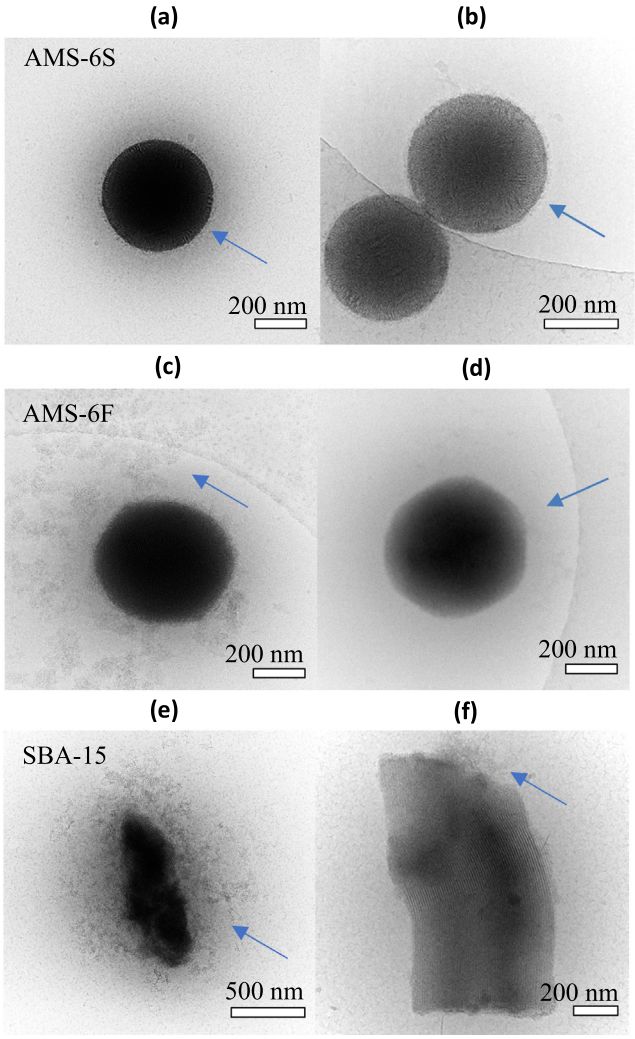

Fig. 6. Cryo-TEM images of MSP-corona complexes showing the presence of a hard PC (bottom images) and a soft PC (top images). Arrows indicate areas of darker contrast associated with proteins bound to the particle. **(a)** T30W1. **(b)** T10W1. **(c)** T10W1. **(d)** T120W3. **(e)** T10W3. **(f)** T30W3.

takin the particle morphology into account. Particles that are used for advanced drug delivery purposes with low agglomeration and immunological stealth should be favourable for intravenous administration of advanced therapies where undesired aggregation can lead to a decrease in blood circulation time and accumulation in non-targeted organs [60].

CRediT authorship contribution statement

Inga Kuschnerus: Conceptualization, Methodology, Writing – original draft, Data curation. **Kalpeshkumar Giri:** Data curation. **Juanfang Ruan:** Data curation. **Yanan Huang:** Data curation. **Nicholas Bedford:** Data curation. **Alfonso Garcia-Bennett:** Conceptualization, Methodology, Writing – original draft, Data curation.

Declaration of Competing Interest

The authors declare that they have no known competing financial interests or personal relationships that could have appeared to influence the work reported in this paper.

Acknowledgement

We are extremely grateful for funding from Australia's Nuclear Science and Technology Organization for access to the Australian Synchrotron (AS183/SAXS/14099). We would like to acknowledge the help of Dr Tim Ryan with sample preparation and analysis at the SAXS beamline of the Australian Synchrotron. The work was also financed through support from the ARC Centre of Excellence for Nanoscale and BioPhotonics (CE140100003), an ARC Future Fellowship (AEGB, FT150100342), as well as a Macquarie University Infrastructure grant (MQRIGB 9201501951). This research has been facilitated by access to Australian Proteome Analysis Facility (APAF, Macquarie University), which is funded by an initiative of the Australian Government as part of the National Collaborative Research Infrastructure Strategy. Dr Juanfang Ruan thanks the Electron Microscopy Unit at UNSW, Sydney.

Appendix A. Supplementary data

Supplementary data to this article can be found online at https://doi.org/10.1016/j.jcis.2021.12.161.

References

[1] J.L. Paris, M. Colilla, I. Izquierdo-Barba, M. Manzano, M. Vallet-Regí, Tuning mesoporous silica dissolution in physiological environments: a review, J. Mater. Sci. 52 (15) (2017) 8761–8771.
[2] S. Heidegger, D. Gößl, A. Schmidt, S. Niedermayer, C. Argyo, S. Endres, T. Bein, C. Bourquin, Immune response to functionalized mesoporous silica nanoparticles for targeted drug delivery, Nanoscale 8 (2) (2016) 938–948.
[3] C. Argyo, V. Weiss, C. Bräuchle, T. Bein, Multifunctional Mesoporous Silica Nanoparticles as a Universal Platform for Drug Delivery, Chem. Mater. 26 (1) (2014) 435–451.
[4] A.E. Garcia-Bennett, M. Kozhevnikova, N. Konig, C. Zhou, R. Leao, T. Knopfel, S. Pankratova, C. Trolle, V. Berezin, E. Bock, H. Aldskogius, E.N. Kozlova, Delivery of differentiation factors by mesoporous silica particles assists advanced differentiation of transplanted murine embryonic stem cells, Stem Cells Transl Med 2 (11) (2013) 906–915.

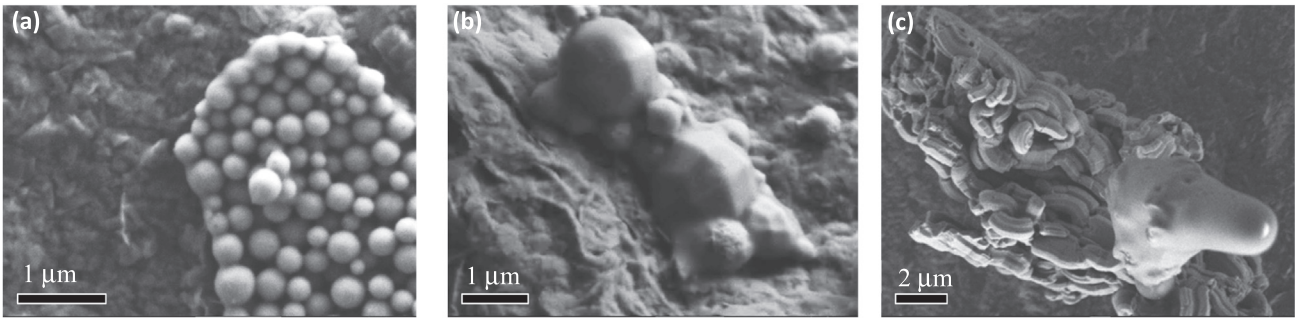

Fig. 7. SEM images of MSP-corona complexes showing the presence of a PC for MSP-corona complexes prepared for **(a)** $T_{120}W_1$ for AMS-6S, **(b)** $T_{120}W_3$ for AMS-6F, and **(c)** $T_{10}W_1$ for SBA-15.

[5] A.E. Garcia-Bennett, Synthesis, toxicology and potential of ordered mesoporous materials in nanomedicine, Nanomedicine 6 (5) (2011) 867–877.
[6] A. Almomen, A.M. El-Toni, M. Badran, A. Alhowyan, M. Abul Kalam, A. Alshamsan, M. Alkholief, The Design of Anionic Surfactant-Based Amino-Functionalized Mesoporous Silica Nanoparticles and their Application in Transdermal Drug Delivery, Pharmaceutics 12 (11) (2020) 1035.
[7] F.S.C. Rodrigues, A. Campos, J. Martins, A.F. Ambrósio, E.J. Campos, Emerging Trends in Nanomedicine for Improving Ocular Drug Delivery: Light-Responsive Nanoparticles, Mesoporous Silica Nanoparticles, and Contact Lenses, ACS Biomater. Sci. Eng. 6 (12) (2020) 6587–6597.
[8] D. Hargrove, B. Liang, R. Kashfi-Sadabad, G.N. Joshi, L. Gonzalez-Fajardo, S. Glass, M. Jay, A. Salner, X. Lu, Tumor-mesoporous silica nanoparticle interactions following intraperitoneal delivery for targeting peritoneal metastasis, J. Control. Release 328 (2020) 846–858.
[9] D. Docter, D. Westmeier, M. Markiewicz, S. Stolte, S.K. Knauer, R.H. Stauber, The nanoparticle biomolecule corona: lessons learned - challenge accepted?, Chem Soc. Rev. 44 (17) (2015) 6094–6121.
[10] S. Tenzer, D. Docter, J. Kuharev, A. Musyanovych, V. Fetz, R. Hecht, F. Schlenk, D. Fischer, K. Kiouptsi, C. Reinhardt, K. Landfester, H. Schild, M. Maskos, S.K. Knauer, R.H. Stauber, Rapid formation of plasma protein corona critically affects nanoparticle pathophysiology, Nat. Nanotechnol. 8 (10) (2013) 772–781.
[11] A.E. Garcia-Bennett, L. Ballell, Non-absorbable mesoporous silica for the development of protein sequestration therapies, Biochem. Biophys. Res. Commun. 468 (3) (2015) 428–434.
[12] N. Kupferschmidt, X. Xia, R.H. Labrador, R. Atluri, L. Ballell, A.E. Garcia-Bennett, In vivo oral toxicological evaluation of mesoporous silica particles, Nanomedicine 8 (1) (2013) 57–64.
[13] A.J. Paula, R.T. Araujo Júnior, D.S.T. Martinez, E.J. Paredes-Gamero, H.B. Nader, N. Durán, G.Z. Justo, O.L. Alves, Influence of protein corona on the transport of molecules into cells by mesoporous silica nanoparticles, ACS Appl. Mater. Interfaces 5 (17) (2013) 8387–8393.
[14] E. Witasp, N. Kupferschmidt, L. Bengtsson, K. Hultenby, C. Smedman, S. Paulie, A.E. Garcia-Bennett, B. Fadeel, Efficient internalization of mesoporous silica particles of different sizes by primary human macrophages without impairment of macrophage clearance of apoptotic or antibody-opsonized target cells, Toxicol. Appl. Pharmacol. 239 (3) (2009) 306–319.
[15] H. Vallhov, S. Gabrielsson, M. Strømme, A. Scheynius, A.E. Garcia-Bennett, Mesoporous silica particles induce size dependent effects on human dendritic cells, NANO Letters 7 (12) (2007) 3576–3582.
[16] D. Tarn, C.E. Ashley, M. Xue, E.C. Carnes, J.I. Zink, C.J. Brinker, Mesoporous Silica Nanoparticle Nanocarriers: Biofunctionality and Biocompatibility, Acc. Chem. Res. 46 (3) (2013) 792–801.
[17] J. Lu, M. Liong, J. Zink, F. Tamanoi, Mesoporous silica nanoparticles as a delivery system for hydrophobic anticancer drugs, Small 3 (8) (2007) 1341–1346.
[18] L. Harini, S. Srivastava, G.P. Gnanakumar, B. Karthikeyan, C. Ross, V. Krishnakumar, V.R. Kannan, K. Sundar, T. Kathiresan, An ingenious non-spherical mesoporous silica nanoparticle cargo with curcumin induces mitochondria-mediated apoptosis in breast cancer (MCF-7) cells, Oncotarget 10 (11) (2019) 1193–1208.
[19] P. Decuzzi, B. Godin, T. Tanaka, S.-Y. Lee, C. Chiappini, et al., Size and shape effects in the biodistribution of intravascularly injected particles. 141 (3) (2010) 320–327.
[20] L. Li, T. Liu, C. Fu, L. Tan, X. Meng, H. Liu, Biodistribution, excretion, and toxicity of mesoporous silica nanoparticles after oral administration depend on their shape, Nanomed.: Nanotechnol. Biol. Med. 11 (8) (2015) 1915–1924.
[21] J.Y. Oh, H.S. Kim, L. Palanikumar, E.M. Go, B. Jana, S.A. Park, H.Y. Kim, K. Kim, J. K. Seo, S.K. Kwak, C. Kim, S. Kang, J.-H. Ryu, Cloaking nanoparticles with protein corona shield for targeted drug delivery, Nat. Commun. 9 (1) (2018) 4548.
[22] C. Vidaurre-Agut, E. Rivero-Buceta, E. Romaní-Cubells, A.M. Clemments, C.D. Vera-Donoso, C.C. Landry, P. Botella, Protein Corona over Mesoporous Silica Nanoparticles: Influence of the Pore Diameter on Competitive Adsorption and Application to Prostate Cancer Diagnostics, ACS Omega 4 (5) (2019) 8852–8861.
[23] A.M. Clemments, C. Muniesa, C.C. Landry, P. Botella, Effect of surface properties in protein corona development on mesoporous silica nanoparticles, RSC Adv. 4 (55) (2014) 29134–29138.
[24] A. Gallud, O. Bondarenko, N. Feliu, N. Kupferschmidt, R. Atluri, A. Garcia-Bennett, B. Fadeel, Macrophage activation status determines the internalization of mesoporous silica particles of different sizes: Exploring the role of different pattern recognition receptors, Biomaterials 121 (2017) 28–40.
[25] O. Bondarenko, N.F. Torres, N. Kupferschmidt, A. Garcia-Bennett, B. Fadeel, Cellular uptake of mesoporous silica particles is governed by activation state of macrophages, Toxicol. Lett. 229 (2014) S188, https://doi.org/10.1016/j.toxlet.2014.06.638.
[26] R. Madathiparambil Visalakshan, L.E. González García, M.R. Benzigar, A. Ghazaryan, J. Simon, A. Mierczynska-Vasilev, T.D. Michl, A. Vinu, V. Mailänder, S. Morsbach, K. Landfester, K. Vasilev, The Influence of Nanoparticle Shape on Protein Corona Formation, Small 16 (25) (2020) 2000285, https://doi.org/10.1002/smll.v16.2510.1002/smll.202000285.
[27] Y.-S. Lin, N. Abadeer, C.L. Haynes, Stability of small mesoporous silica nanoparticles in biological media, Chem. Commun. (Camb) 47 (1) (2011) 532–534.
[28] S.R. Blumen, K. Cheng, M.E. Ramos-Nino, D.J. Taatjes, D.J. Weiss, C.C. Landry, B. T. Mossman, Unique uptake of acid-prepared mesoporous spheres by lung epithelial and mesothelioma cells, Am. J. Respir. Cell Mol. Biol. 36 (3) (2007) 333–342.
[29] Z. Ma, J. Bai, Y. Wang, X. Jiang, Impact of Shape and Pore Size of Mesoporous Silica Nanoparticles on Serum Protein Adsorption and RBCs Hemolysis, ACS Appl. Mater. Interfaces 6 (4) (2014) 2431–2438.
[30] A.M. Clemments, P. Botella, C.C. Landry, Protein Adsorption From Biofluids on Silica Nanoparticles: Corona Analysis as a Function of Particle Diameter and Porosity, ACS Appl. Mater. Interfaces 7 (39) (2015) 21682–21689.
[31] J. Saikia, M. Yazdimamaghani, S.P. Hadipour Moghaddam, H. Ghandehari, Differential Protein Adsorption and Cellular Uptake of Silica Nanoparticles Based on Size and Porosity, ACS Appl. Mater. Interfaces 8 (50) (2016) 34820–34832.
[32] K. Giri, I. Kuschnerus, M. Lau, J. Ruan, A. Garcia-Bennett, Pore structure and particle shape modulates the protein corona of mesoporous silica particles, Mater. Adv. 1 (4) (2020) 599–603.
[33] A.C.G. Weiss, H.G. Kelly, M. Faria, Q.A. Besford, A.K. Wheatley, C.-S. Ang, E.J. Crampin, F. Caruso, S.J. Kent, Link between Low-Fouling and Stealth: A Whole Blood Biomolecular Corona and Cellular Association Analysis on Nanoengineered Particles, ACS Nano 13 (5) (2019) 4980–4991.
[34] A.N. Ilinskaya, M.A. Dobrovolskaia, Nanoparticles and the blood coagulation system Part II: safety concerns, Nanomedicine (Lond.) 8 (6) (2013) 969–981.
[35] K. Sun, T. Ding, Y. Xing, D. Mo, J. Zhang, J.M. Rosenholm, Hybrid mesoporous nanorods with deeply grooved lateral faces toward cytosolic drug delivery, Biomater. Sci. 7 (12) (2019) 5301–5311.
[36] K. Giri, I. Kuschnerus, J. Ruan, A.E. Garcia-Bennett, Influence of a Protein Corona on the Oral Pharmacokinetics of Testosterone Released from Mesoporous Silica, Adv. Therapeutics 3 (5) (2020) 1900110, https://doi.org/10.1002/adtp.v3.510.1002/adtp.201900110.
[37] M. Lau, K. Giri, A.E. Garcia-Bennett, Antioxidant properties of probucol released from mesoporous silica, Eur. J. Pharm. Sci. 138 (2019) 105038, https://doi.org/10.1016/j.ejps.2019.105038.
[38] A. Berardi, F. Baldelli Bombelli, Oral delivery of nanoparticles - let's not forget about the protein corona, Expert Opinion on Drug Delivery 16 (6) (2019) 563–566.
[39] S. Ritz, S. Schöttler, N. Kotman, G. Baier, A. Musyanovych, J. Kuharev, K. Landfester, H. Schild, O. Jahn, S. Tenzer, V. Mailänder, Protein corona of nanoparticles: distinct proteins regulate the cellular uptake, Biomacromolecules 16 (4) (2015) 1311–1321.
[40] S. Sheibani, K. Basu, A. Farnudi, A. Ashkarran, M. Ichikawa, J.F. Presley, K.H. Bui, M.R. Ejtehadi, H. Vali, M. Mahmoudi, Nanoscale characterization of the biomolecular corona by cryo-electron microscopy, cryo-electron tomography, and image simulation, Nat. Commun. 12 (1) (2021) 573.
[41] I. Yadav, V.K. Aswal, J. Kohlbrecher, Size-dependent interaction of silica nanoparticles with lysozyme and bovine serum albumin proteins, Phys. Rev. E 93 (5) (2016) 052601.
[42] K. Lund, A.E. Garcia-Bennett, O. Terasaki, On the use of polymeric dispersant P123 in the synthesis of bicontinuous cubic mesoporous AMS-6, J. Mater. Chem. 17 (34) (2007) 3622–3629.
[43] S. Che, K. Lund, T. Tatsumi, S. Iijima, S.H. Joo, R. Ryoo, O. Terasaki, Direct Observation of 3D Mesoporous Structure by Scanning Electron Microscopy (SEM): SBA-15 Silica and CMK-5 Carbon, Angewandte Chemie International Edition 42 (19) (2003) 2182–2185.
[44] R. Atluri, N. Hedin, A.E. Garcia-Bennett, Hydrothermal Phase Transformation of Bicontinuous Cubic Mesoporous Material AMS-6, Chem. Mater. 20 (12) (2008) 3857–3866.
[45] L.u. Han, T. Ohsuna, Z. Liu, V. Alfredsson, T. Kjellman, S. Asahina, M. Suga, Y. Ma, P. Oleynikov, K. Miyasaka, A. Mayoral, I. Díaz, Y. Sakamoto, S.M. Stevens, M.W. Anderson, C. Xiao, N. Fujita, A. Garcia-Bennett, K. Byung Yoon, S. Che, O. Terasaki, Structures of silica-based nanoporous materials revealed by microscopy, Zeitschrift fur Anorganische und Allgemeine Chemie 640 (3-4) (2014) 521–536.
[46] P. Arenas-Guerrero, Á.V. Delgado, K.J. Donovan, K. Scott, T. Bellini, F. Mantegazza, M.L. Jiménez, Determination of the size distribution of non-spherical nanoparticles by electric birefringence-based methods, Sci. Rep. 8 (1) (2018) 9502.
[47] J. Schmitt, C. Hartwig, J.J. Crassous, A.M. Mihut, P. Schurtenberger, V. Alfredsson, Anisotropic mesoporous silica/microgel core–shell responsive particles, RSC Adv. 10 (42) (2020) 25393–25401.
[48] J. Ilavsky, P.R. Jemian, Irena: Tool Suite for Modeling and Analysis of Small Angle Scattering, J. Appl. Crystallography - J APPL CRYST 42 (2) (2009) 347–353.
[49] F. Spinozzi, G. Ceccone, P. Moretti, G. Campanella, C. Ferrero, S. Combet, I. Ojea-Jimenez, P. Ghigna, Structural and Thermodynamic Properties of Nanoparticle-Protein Complexes: A Combined SAXS and SANS Study, Langmuir 33 (9) (2017) 2248–2256.
[50] T. Li, A.J. Senesi, B. Lee, Small Angle X-ray Scattering for Nanoparticle Research, Chem. Rev. 116 (18) (2016) 11128–11180.
[51] L.u. Han, N. Fujita, H. Chen, C. Jin, O. Terasaki, S. Che, Crystal twinning of bicontinuous cubic structures, IUCrJ 7 (2) (2020) 228–237.
[52] M. Wiśniewska, K. Szewczuk-Karpisz, D. Sternik, Adsorption and thermal properties of the bovine serum albumin–silicon dioxide system, J. Thermal Anal. Calorimetry 120 (2) (2015) 1355–1364.

[53] I.M. Weiss, C. Muth, R. Drumm, H.O.K. Kirchner, Thermal decomposition of the amino acids glycine, cysteine, aspartic acid, asparagine, glutamic acid, glutamine, arginine and histidine, BMC Biophysics 11 (1) (2018) 2.
[54] A. Chrzanowska, A. Derylo-Marczewska, Mesoporous silica/protein biocomposites: Surface, topography, thermal properties, Int. J. Biol. Macromol. 139 (2019) 531–542.
[55] A.E. Garcia-Bennett, A. Everest-Dass, I. Moroni, I.D. Rastogi, L.M. Parker, N.H. Packer, L.J. Brown, Influence of surface chemistry on the formation of a protein corona on nanodiamonds, J. Mater. Chem. B 7 (21) (2019) 3383–3389.
[56] A. Katiyar, L. Ji, P. Smirniotis, N.G. Pinto, Protein adsorption on the mesoporous molecular sieve silicate SBA-15: effects of pH and pore size, J. Chromatogr. A 1069 (1) (2005) 119–126.
[57] W.H. Stein, S. Moore, Amino acid composition of beta-lactoglobulin and bovine serum albumin, J. Biol. Chem. 178 (1) (1949) 79–91.
[58] B. Fazio, C. D'Andrea, A. Foti, E. Messina, A. Irrera, M.G. Donato, V. Villari, N. Micali, O.M. Maragò, P.G. Gucciardi, SERS detection of Biomolecules at Physiological pH via aggregation of Gold Nanorods mediated by Optical Forces and Plasmonic Heating, Sci. Rep. 6 (2016) 26952.
[59] M. Kokkinopoulou, J. Simon, K. Landfester, V. Mailänder, I. Lieberwirth, Visualization of the protein corona: towards a biomolecular understanding of nanoparticle-cell-interactions, Nanoscale 9 (25) (2017) 8858–8870.
[60] J. Meissner, A. Prause, B. Bharti, G.H. Findenegg, Characterization of protein adsorption onto silica nanoparticles: influence of pH and ionic strength, Colloid Polym. Sci. 293 (11) (2015) 3381–3391.
[61] Y. Qi, T. Zhang, C. Jing, S. Liu, C. Zhang, P.J.J. Alvarez, W. Chen, Nanocrystal facet modulation to enhance transferrin binding and cellular delivery, Nat. Commun. 11 (1) (2020) 1262.
[62] S.K. Ramakrishnan, M. Martin, T. Cloitre, L. Firlej, F.J.G. Cuisinier, C. Gergely, Insights on the facet specific adsorption of amino acids and peptides toward platinum, J. Chem. Inf. Model. 53 (12) (2013) 3273–3279.